The Astrophysical Journal, 1000:239 (10pp), 2026 April 1 https://doi.org/10.3847/1538-4357/ae4ec0

Stability and Characteristics of Lower-hybrid Drift Waves: Dependence on Electron Beta and Cross-field Relative Drift

Jongsoo Yoo[1], Hantao Ji[2], Jonathan Ng[3], Li-Jen Chen[4], Peiyun Shi[1], Sayak Bose[1], Kush Maheshwari[2], Euichan Jung[2], and Adam Robbins[2]
[1] Princeton Plasma Physics Laboratory, USA; jyoo@pppl.gov
[2] Princeton University, Department of Astrophysical Sciences, USA
[3] University of Maryland, Department of Astronomy, USA
[4] NASA Goddard Space Flight Center, USA
Received 2025 October 22; revised 2026 February 6; accepted 2026 March 5; published 2026 March 26

Abstract

Lower-hybrid drift waves (LHDWs) are frequently observed microinstabilities in both space and laboratory plasmas. Despite decades of study, the relationship between electrostatic (ES-LHDW) and electromagnetic (EM-LHDW) variants and the plasma parameters controlling their stability remains unclear. Here, we systematically examine LHDW behavior by solving the local linear dispersion relation over a wide range of plasma and field conditions. Our results demonstrate that ES-LHDWs and EM-LHDWs are not distinct modes but rather two different regimes of the same drift wave whose character evolves smoothly with electron beta (β_e) and the cross-field electron drift velocity relative to ions, normalized to the ion sound speed (u_{0x}/C_s). The nature of the waves changes from electrostatic to electromagnetic when β_e increases. Growth rates increase with u_{0x}/C_s but decrease with β_e, while the most unstable wavelength remains nearly universal, with $k\rho_e \sim 0.8$ (k is the magnitude of the wave vector and ρ_e is the electron gyroradius). We further present quasi-linear estimates of nonlinear saturation properties, including energy partition among electric fields, magnetic fields, and particle kinetic responses. We show that ES-LHDWs reach higher electric-field saturation amplitudes, whereas EM-LHDWs generate strong magnetic perturbations and parallel electric fields that may enable efficient particle heating. Comparisons with the classical model reveal that retaining electromagnetic effects is essential for accurate predictions of frequency, growth rate, and the propagation angle. These findings provide a unified framework for understanding LHDWs across diverse collisionless plasma environments, including current sheets of magnetic reconnection, shear layers, collisionless shocks, and boundary regions.

Unified Astronomy Thesaurus concepts: Solar magnetic reconnection (1504); Solar physics (1476); Solar coronal waves (1995)

1. Introduction

Lower hybrid drift waves (LHDWs) are among the most frequently observed microinstabilities in strongly inhomogeneous plasmas, including space environments (e.g., S. D. Bale et al. 2002; P. K. Shukla & A. A. Mamun 2002; C. Norgren et al. 2012; D. B. Graham et al. 2017, 2019; L.-J. Chen et al. 2019, 2020; J. Yoo et al. 2020; D. B. Graham et al. 2022; Z. Z. Guo et al. 2022; Z. Ouyang et al. 2022; N. Ahmadi et al. 2025) and laboratory experiments (e.g., T. A. Carter et al. 2001; H. Ji et al. 2004; J. Yoo et al. 2014, 2024, 2025). They have long been considered a candidate mechanism for anomalous transport because of their interactions with magnetized electrons and unmagnetized ions, which enable momentum exchange between the two species (e.g., T. A. Carter et al. 2001; H. Ji et al. 2004; R. Kulsrud et al. 2005; I. Silin et al. 2005; P. H. Yoon & A. T. Y. Lui 2007; V. Roytershteyn et al. 2012, 2013; J. Yoo et al. 2020). Their importance lies in their ability to grow rapidly on the cross-field electron-ion drift and to mediate momentum transfer in collisionless plasmas (P. H. Yoon & A. T. Y. Lui 2004).

In collisionless current sheets of magnetic reconnection, LHDWs are commonly observed near regions of strong density gradients. During magnetic reconnection, for example, they have been linked to electron heating, vortical flows, and anomalous resistivity (L.-J. Chen et al. 2020; J. Yoo et al. 2020; D. B. Graham et al. 2022; J. Yoo et al. 2024, 2025; B. Feng et al. 2025). However, their occurrence is not limited to reconnection: LHDWs are also important in turbulent boundary layers, collisionless shocks, planetary magnetospheres, the solar wind, and the corona (W. Daughton 2003; R. A. Treumann 2009; D. B. Graham et al. 2019).

Two seemingly distinct classes of LHDWs are often discussed in the literature. The first is the quasi-electrostatic form (ES-LHDW), identified in early theoretical work (e.g., R. Davidson et al. 1977; T. Carter et al. 2002b) and later confirmed in laboratory, space, and simulation studies (e.g., T. Carter et al. 2002a; V. Roytershteyn et al. 2012; J. Yoo et al. 2014, 2017, 2024, 2025; N. Ahmadi et al. 2025). ES-LHDWs typically arise at low electron beta, propagate nearly perpendicular to the magnetic field, and are characterized by strong electric field fluctuations. They are often observed near low-density separatrices or sharp boundary layers, especially in the absence of strong guide fields.

The second is the electromagnetic LHDW (EM-LHDW), reported in laboratory, space, and simulation studies (H. Ji et al. 2004; V. Roytershteyn et al. 2012; J. Yoo et al. 2020; N. Ahmadi et al. 2025). EM-LHDWs are more prevalent at higher β_e, propagate obliquely to the magnetic field, and exhibit strong magnetic fluctuations. These waves are typically

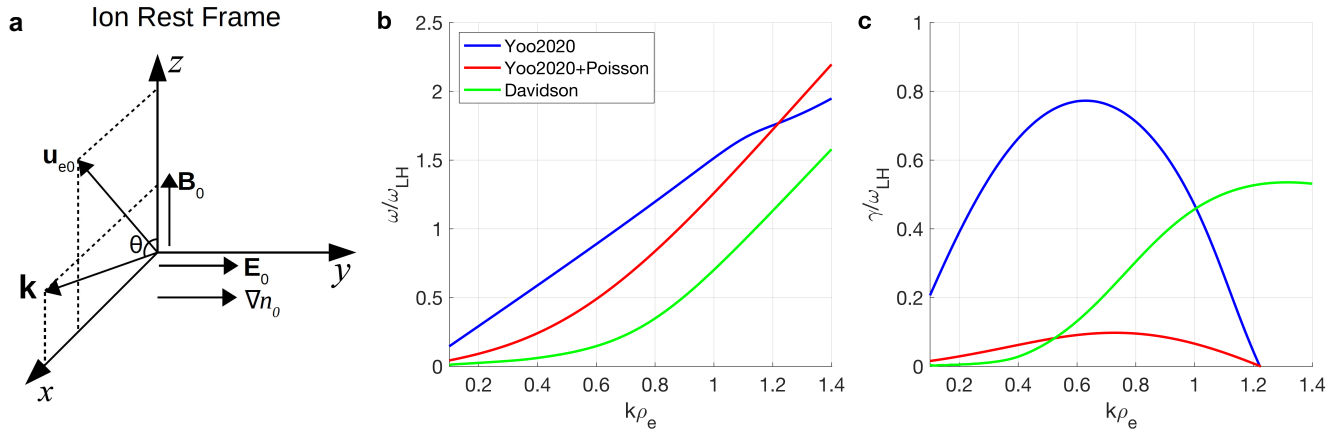

Figure 1. Local theoretical model and benchmarking. The plasma and field parameters are the same as those of the reference case, with $\beta_e = 0.5$ and $u_{0x}/C_s = 4.1$. (a) Geometry of the local, linear model. Calculations are performed in the ion rest frame with $\boldsymbol{B}_0$ along z, the density gradient along y, and electron drift $\boldsymbol{u}_{e0}$ in the x–z plane. The wavevector $\boldsymbol{k}$ makes an angle θ with $\boldsymbol{B}_0$, with no propagation along y. (b) Real frequency ω/ω_{LH} and (c) growth rate γ/ω_{LH} as functions of $k\rho_e$ for three formulations with $\theta = 90°$: the present model (blue), the classical model of R. Davidson et al. (1977; green), and a simplified model using Poisson's equation in place of Faraday's law (red). Compared to the classical solution, the present model yields a more linear dispersion and a peak growth rate at smaller $k\rho_e < 1.0$. Substituting Poisson's equation partially restores agreement with the classical model but underestimates the growth rate. These results demonstrate that including Faraday's induction term is essential to capture the correct LHDW physics.

found inside the electron diffusion region without a guide field, and their contribution to sustaining the reconnection electric field under magnetospheric conditions has been investigated (H. Ji et al. 2005; R. Kulsrud et al. 2005; V. Roytershteyn et al. 2012; N. Ahmadi et al. 2025) with typical plasma and field parameters of Earth's magnetosphere.

In this study, we systematically investigate the parameter dependence of LHDW stability and characteristics by solving the dispersion relation under a broad range of conditions using local linear theory without collisions (J. Yoo et al. 2020), generalized from an earlier version (H. Ji et al. 2005) to incorporate electrostatic effects. Our results clarify the conditions under which stability and wave properties change, thereby resolving longstanding misconceptions and providing a unified framework for interpreting LHDWs. In particular, we demonstrate that ES-LHDWs and EM-LHDWs are not distinct modes, but rather two different types of the same drift wave whose properties vary continuously with plasma and field parameters. We further show that their characteristic wavelengths, often described as $k\rho_e \sim 1$ (for ES-LHDWs) and $k\sqrt{\rho_e\rho_i} \sim 1$ (for EM-LHDWs), are in fact comparable, with EM-LHDWs exhibiting only a slight shift toward larger scales under typical conditions. Finally, we identify two key control parameters: the electron beta ($\beta_e = n_e T_e/(0.5B^2/\mu_0)$) (J. Yoo et al. 2020; N. Ahmadi et al. 2025), where n_e is the electron density, T_e the electron temperature, B the magnetic field strength, and μ_0 the vacuum permeability and the perpendicular electron drift velocity (u_{0x}) normalized to the ion sound speed ($C_s = \sqrt{T_e/m_i}$; m_i is the ion mass). This work provides a unified basis for interpreting LHDWs across diverse plasma environments, from space and astrophysical systems to laboratory experiments.

2. Geometry of Local Linear Model

Figure 1(a) illustrates the geometry of our local, linear theoretical model used to solve the LHDW dispersion relation. Here, the subscript 0 denotes equilibrium quantities. Calculations are performed in the ion rest frame, so that electrons drift with velocity $\boldsymbol{u}_{e0}$ in the x–z plane. The Cartesian coordinates are defined such that the equilibrium magnetic field $\boldsymbol{B}_0$ lies along the z-direction, the equilibrium density gradient points along the y-direction, and the wavevector $\boldsymbol{k}$ makes an angle θ with $\boldsymbol{B}_0$. Because the model is local, we neglect wave propagation along the y (gradient)-direction. The governing dispersion relation, along with a detailed derivation, is provided in the Supporting Information of J. Yoo et al. (2020).

It is instructive to relate this local coordinate system to the geometry of magnetic reconnection. In the high-guide field limit, the magnetic field near the electron diffusion region is dominated by the out-of-plane component. In this case, $\boldsymbol{e}_z$ (the unit vector along z) approximately coincides with the out-of-plane, symmetric direction. The perpendicular current is carried primarily by electron outflows, which align $\boldsymbol{e}_x$ with the outflow direction. The density gradient direction $\boldsymbol{e}_y$ then points normal to the current sheet.

In contrast, when the guide field is negligible, the reconnecting magnetic field component becomes dominant. Here, $\boldsymbol{e}_z$ aligns with the outflow direction, while the perpendicular current is dominated by the out-of-plane component, setting $\boldsymbol{e}_x$ along that direction. As in the high-guide field case, $\boldsymbol{e}_y$ continues to represent the normal to the current sheet. This mapping clarifies how the local linear model can be used to study reconnecting current sheets in both limits.

For quantitative analysis, we adopt plasma and magnetic field parameters typical of Earth's magnetopause current sheets (J. Yoo et al. 2020). The baseline values are: local density $n_0 = 5\ \mathrm{cm}^{-3}$, equilibrium magnetic field strength $B_0 = 20\ \mathrm{nT}$, electron and ion temperatures $T_e = T_i = 100\ \mathrm{eV}$, perpendicular electron flow velocity $u_{0x} = 400\ \mathrm{km\,s}^{-1}$, and parallel electron flow velocity $u_{0z} = -400\ \mathrm{km\,s}^{-1}$. These values, summarized in Table 1, are used as the reference case throughout this study.

Because our model introduces several modifications compared with earlier approaches, it is essential to benchmark its predictions against a well-established classical framework. We therefore compare with the model of R. Davidson et al. (1977), which restricts the wavevector to $\theta = 90°$ and neglects parallel

Table 1
Summary of Parameters for Dispersion Relation Calculations

Parameter	Reference	Case 1	Case 2	Case 3	Case 4	Case 5	Case 6	Case 7
n_0 (cm^3)	5	50	5	5	5	5	5	5
B_0 (nT)	20	20	6.32	20	20	20	20	20
T_i (eV)	100	100	100	1000	200	100	100	100
$T_{e\|\|}$ (eV)	100	100	100	1000	100	200	200	100
$T_{e\perp}$ (eV)	100	100	100	1000	100	200	100	200
β_e	0.5	5.0	5.0	5.0	0.5	1.0	0.84	0.67
u_{0x}/C_s	4.1	4.1	4.1	1.3	4.1	2.9	3.2	3.5

Note. In all cases, the physical value of u_{0x} and u_{0z} is fixed at 400 and -400 km s^{-1}, respectively.

electron drift ($u_{0z} = 0$). To enable a direct comparison, we solve our dispersion relation under the same assumptions.

Despite the common setup, the governing equations in the two models differ in important ways. In the classical formulation, electrostatic fluctuations are obtained from Poisson's equation, whereas our model incorporates Faraday's induction law (H. Ji et al. 2005), thereby retaining the full electromagnetic effects. To isolate the consequences of this difference, we constructed a hybrid formulation that uses Poisson's equation (as in the classical model) in place of Faraday's law, while retaining our updated expressions for the perturbed density and current density. (J. Yoo et al. 2022)

Figures 1(b) and (c) compare the real and imaginary parts of ω/ω_{LH} as functions of $k\rho_e$ for three representative cases. Results from our model (blue lines) differ substantially from those of the classical model (green lines). For the real frequency ω/ω_{LH}, our model predicts an almost linear dependence on $k\rho_e$, whereas in the classical model, the frequency increases more gradually at small $k\rho_e$. A second important difference is in the growth rate: the maximum γ/ω_{LH} in our model occurs near $k\rho_e \sim 0.65$, whereas in the classical model the peak shifts to $k\rho_e \sim 1.3$.

When Poisson's equation is substituted for Faraday's law in our formulation (red lines), the results shift closer to the classical model: the ω/ω_{LH} profile resembles that of the classical solution, and the peak growth rate moves to $k\rho_e \sim 0.8$. This comparison demonstrates that retaining Faraday's induction term (H. Ji et al. 2005), thereby including full electromagnetic effects, is essential for correctly capturing both electrostatic and electromagnetic physics of LHDWs (J. Yoo et al. 2022). This conclusion is supported by both laboratory and space observations (J. Yoo et al. 2014, 2020), which consistently show that electric field fluctuations in ES-LHDWs are accompanied by comparable magnetic field fluctuations.

Finally, Figure 1(c) shows that the growth rate predicted by the simplified model (red lines) is substantially lower than that obtained from the classical model (green). This reduction is likely attributable to the absence of a rigorous heat-flux treatment in the simplified formulation, which limits its ability to fully capture kinetic effects.

3. Results

Table 1 summarizes the plasma and field parameters adopted for all dispersion relation calculations. In every case, the physical values of the electron drift velocities are fixed at $u_{0x} = 400\,\mathrm{km\,s^{-1}}$ and $u_{0z} = -400\,\mathrm{km\,s^{-1}}$. Cases 1–3 are designed to study the effect of the electron beta, β_e, which is increased by a factor of 10 relative to the reference case using three different approaches: (i) by raising the density (Case 1), (ii) by reducing the magnetic field strength (Case 2), and (iii) by increasing the electron temperature while also raising the ion temperature proportionally (Case 3).

The resulting 2D dispersion relations are shown in Figure 2 for the reference case and the three high-β_e cases. In each panel, the left (right) plot displays the real (imaginary) part of ω/ω_{LH} as a function of $k\rho_e$ and the propagation angle θ. For the reference case, the most unstable mode exhibits a large growth rate ($\gamma/\omega_{LH} \sim 0.8$) near $\theta = 90°$, corresponding to ES-LHDWs. This behavior is consistent with expectations for low-β_e plasmas (J. Yoo et al. 2020, 2024, 2025).

When β_e is increased to 5, two distinct responses are observed depending on how the increase is achieved. In the density-increased (Figure 2(b)) and reduced-field (Figure 2(c)) cases, the peak of the unstable mode shifts toward more oblique propagation ($\theta \sim 70°$). Both the normalized frequency (ω/ω_{LH}) and growth rate (γ/ω_{LH}) are significantly reduced compared with the reference case. These trends indicate a change in the character of the mode: the ES-LHDW continuously evolves into an EM-LHDW as β_e increases. Importantly, this should not be interpreted as the stabilization of the ES-LHDW propagating nearly perpendicularly to the local magnetic field (T. Carter et al. 2002b), followed by the excitation of a separate EM-LHDW propagating obliquely to the local magnetic field (H. Ji et al. 2005). Instead, they represent the same mode, whose properties smoothly transition from electrostatic to electromagnetic with increasing β_e (J. Yoo et al. 2020).

By contrast, when β_e is raised through higher electron and ion temperatures (Figure 2(d)), LHDWs are strongly suppressed, and the mode becomes only marginally unstable. This finding highlights that, beyond β_e, an additional dimensionless parameter associated with temperature plays a key role in regulating the stability of LHDWs.

To identify the additional parameter that governs LHDW stability, we next compute the 2D dispersion relations for four more cases (Cases 4–7 in Table 1). Figure 3(a) shows Case 4, in which the ion temperature is doubled. In this case, both the normalized frequency (ω/ω_{LH}) and growth rate (γ/ω_{LH}) remain nearly unchanged compared with the reference case, indicating that LHDWs are largely insensitive to variations in ion temperature.

A different behavior emerges when only the electron temperature is increased (Case 5). As shown in Figure 3(b), both ω/ω_{LH} and γ/ω_{LH} decrease significantly, clearly demonstrating that electron dynamics play the central role in regulating LHDW stability.

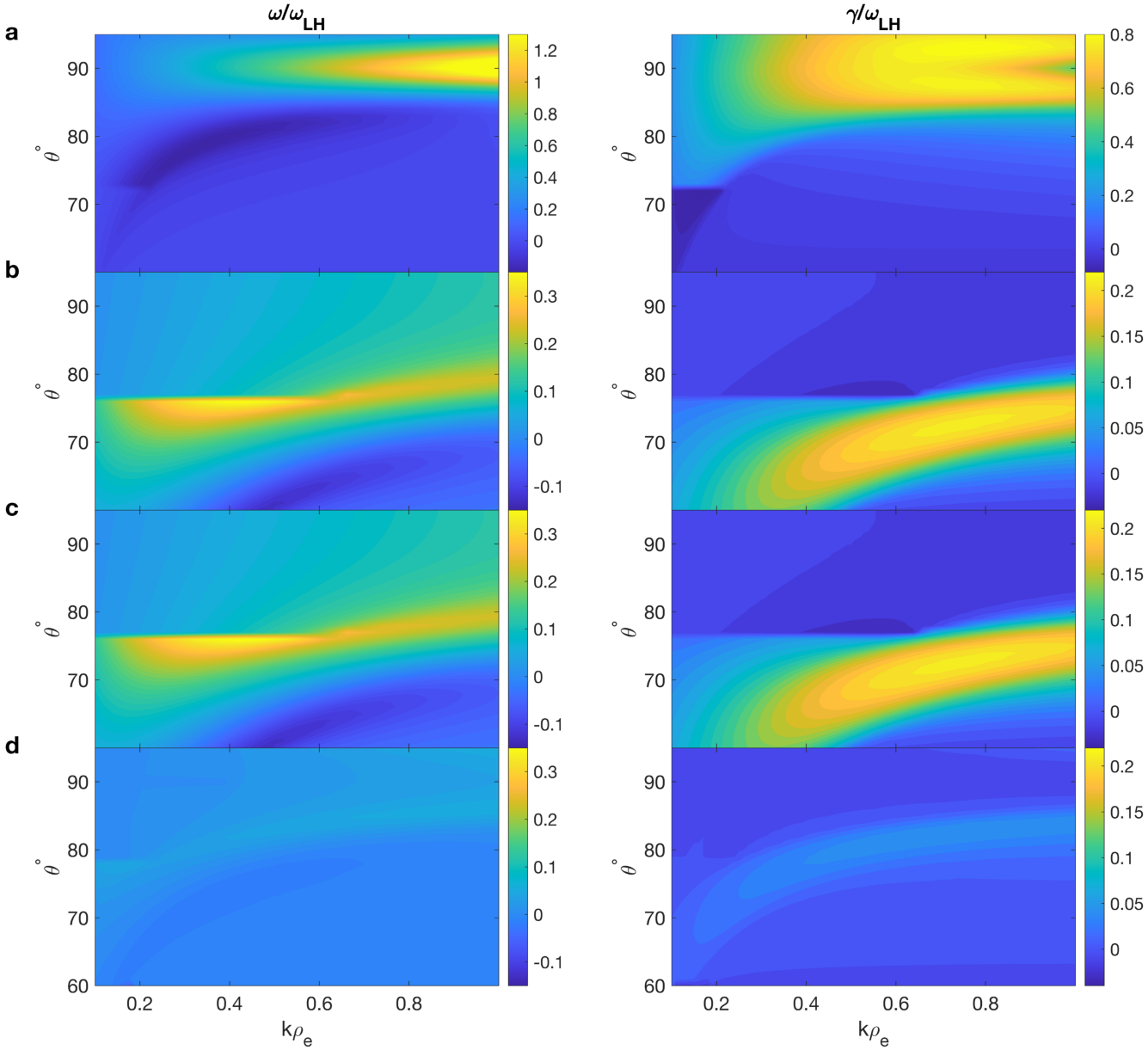

Figure 2. Dispersion relation results for the four cases summarized in Table 1 (reference and Cases 1–3). In each case, the left panels show the real frequency $\omega/\omega_{\rm LH}$ and the right panels show the growth rate $\gamma/\omega_{\rm LH}$ as functions of $k\rho_{\rm e}$ and θ. Note that the range of $\gamma/\omega_{\rm LH}$ is from -1 to 0.8 for the reference case, whereas it is from -0.04 to 0.22 for all other cases. (a) Reference case ($\beta_{\rm e} = 0.5$): the mode is strongly unstable near $k\rho_{\rm e} \sim 0.8$ and $\theta = 90°$, with a maximum frequency of $\omega/\omega_{\rm LH} \sim 0.73$. (b) Case with $\beta_{\rm e} = 5$ obtained by increasing the density: the most unstable mode shifts to $k\rho_{\rm e} \sim 0.76$ and $\theta \sim 73°$, with reduced $\omega/\omega_{\rm LH}$ and $\gamma/\omega_{\rm LH}$, indicating a transition toward EM-LHDW characteristics. (c) Case with $\beta_{\rm e} = 5$ obtained by decreasing the magnetic field: the results are nearly identical to those described in panel (b). (d) Case with $\beta_{\rm e} = 5$ obtained by increasing the temperature: the LHDW becomes only marginally unstable.

To understand the effects of electron temperature anisotropy, we then examine Cases 6 and 7. Note that we define ion sound speed $C_{\rm s} \equiv \sqrt{(2T_{e\perp} + T_{e||})/3m_{\rm i}}$ in these cases. In Case 6, where the perpendicular electron temperature $T_{\rm e\perp}$ is doubled, the most unstable modes shift toward more oblique propagation angles, and modes with negligible $k_{||}$ are stabilized (Figure 3(c)). Because electrons are strongly magnetized for LHDWs, their motion in response to these modes is largely restricted to the $\boldsymbol{E} \times \boldsymbol{B}$ drift. Consequently, the wave-driven density perturbations require a perpendicular compression of electron phase space. An enhanced $T_{\rm e\perp}$ increases the "kinetic stiffness" of the electron fluid: the higher perpendicular thermal pressure opposes this compression, thereby reducing the ability of the wave to organize electrons into coherent cross-field drifts. This effect preferentially stabilizes modes with $k_{||} \sim 0$.

By contrast, in Case 7, where the parallel electron temperature $T_{\rm e||}$ is doubled, nearly all oblique modes are suppressed, leaving only the $k_{||} \sim 0$ modes unstable (Figure 3(d)). The stabilization observed in this case is dominated by parallel Landau damping. As the parallel wavenumber increases, the mode transitions from a purely perpendicular drift wave to an oblique mode, allowing electrons to respond along the magnetic field lines. We find that the mode is stabilized when $k_{\|}\rho_e \gtrsim 0.03$.

This threshold can be quantified by examining the parallel resonance condition associated with the parallel phase velocity, $v_{\rm ph\|} = \omega/k_{\|} \approx v_{\rm te\|}$, where $v_{\rm te\|}$ is the parallel electron

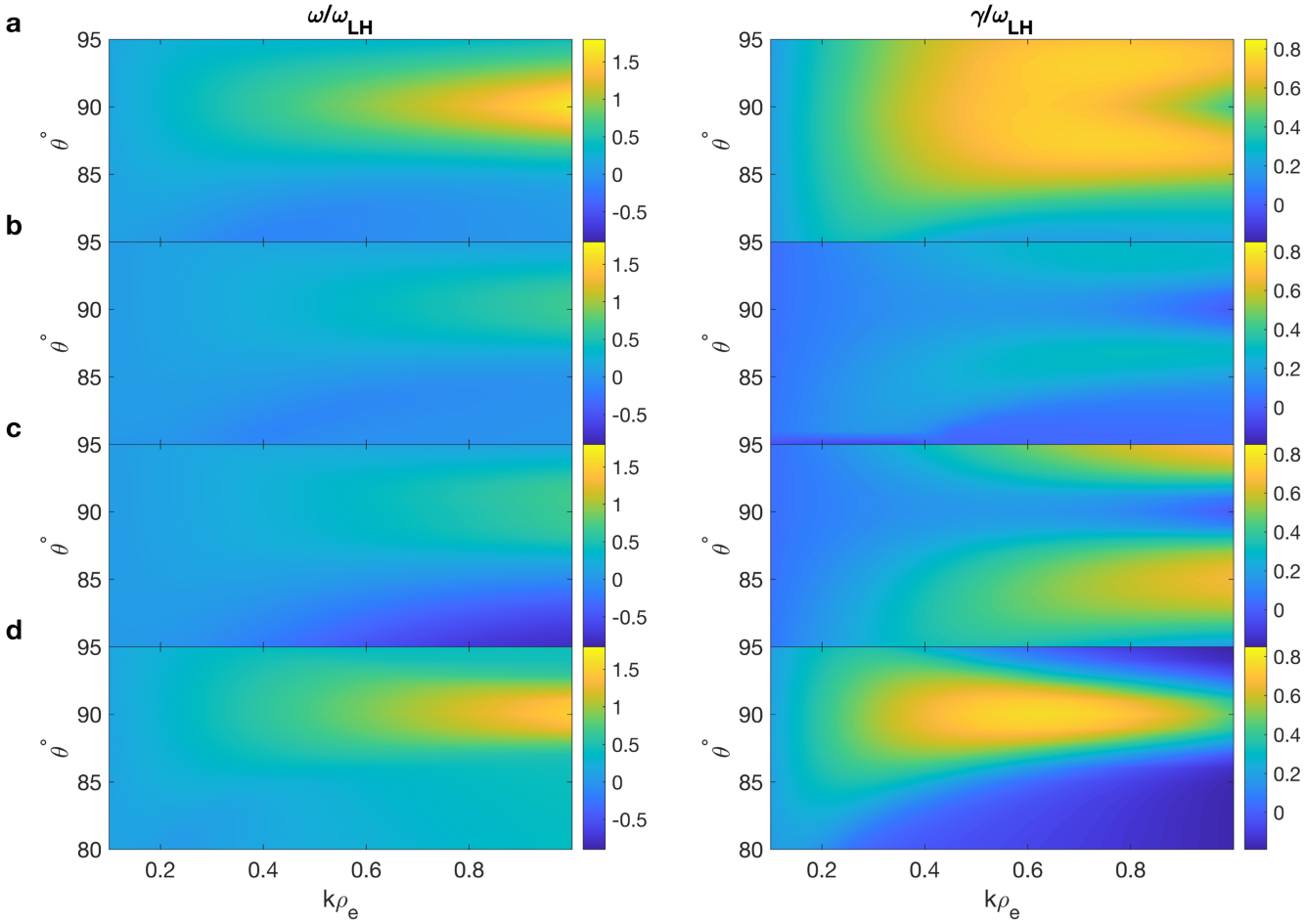

Figure 3. Dispersion relation results for additional cases (Cases 4–7 in Table 1). Left panels show $\omega/\omega_{\rm LH}$, and right panels show $\gamma/\omega_{\rm LH}$ as functions of $k\rho_{\rm e}$ and θ. Note that the range of $\gamma/\omega_{\rm LH}$ is from -0.19 to 0.85 for all cases. (a) When the ion temperature is doubled, both frequency and growth rate remain almost unchanged from the reference case. (b) Doubling the electron temperature produces a significant reduction in both $\omega/\omega_{\rm LH}$ and $\gamma/\omega_{\rm LH}$. (c) When the perpendicular electron temperature is increased, the most unstable modes shift to more oblique angles, while modes with $k_{||} \sim 0$ are stabilized. (d) When the parallel electron temperature is doubled, only modes with $k_{||} \sim 0$ retain positive growth rates, as all others are stabilized by parallel Landau damping.

thermal velocity. Given that the real frequency of the mode is $\omega \approx \omega_{\rm LH}$, this condition can be expressed in terms of the normalized wavenumber as $k_{||}\rho_{\rm e} \approx \omega_{\rm LH}/\omega_{\rm ce} = \sqrt{m_{\rm e}/m_{\rm i}} \simeq 0.023$, in good agreement with the observed stabilization boundary. This provides a clear, quantitative link between the electron thermal distribution and the stability limits of oblique LHDWs. Thus, when both $T_{\rm e||}$ and $T_{\rm e\perp}$ are increased simultaneously, as in Case 5 shown in Figure 3(b), the combined effects act to strongly suppress the overall LHDW growth rate.

Together, these results point to an additional dimensionless control parameter that is directly tied to the electron temperature. At the same time, the parameter must also involve u_{0x}, the perpendicular component of the electron drift velocity in the ion rest frame, since u_{0x} serves as the primary free-energy source for LHDWs (P. H. Yoon & A. T. Y. Lui 2004; J. Yoo et al. 2020, 2022). A natural choice is therefore the ratio $u_{0x}/C_{\rm s}$, where $C_{\rm s} = \sqrt{T_{\rm e}/m_{\rm i}}$ is the ion sound speed. We adopt $C_{\rm s}$ rather than the electron thermal velocity because, under typical conditions, u_{0x} is comparable to $C_{\rm s}$.

With the two key control parameters now identified, we next examine how LHDW stability and wave characteristics vary across β_e and $u_{0x}/C_{\rm s}$. In this analysis, we track the mode with the maximum growth rate as β_e and $u_{0x}/C_{\rm s}$ are varied. Plasma and field parameters are based on the reference case, with the parallel electron drift velocity set to zero for simplicity. Variations in β_e are introduced by changing the magnetic field strength, while $u_{0x}/C_{\rm s}$ is adjusted through u_{0x}.

Figure 4 summarizes the parameter dependence of the most unstable mode. As shown in Figure 4(a), the normalized maximum growth rate ($\gamma_{\rm max}/\omega_{\rm LH}$) increases with $u_{0x}/C_{\rm s}$ but decreases with β_e. The first trend is straightforward: stronger perpendicular drifts provide more free energy to drive LHDWs. The second trend indicates that ES-LHDWs generally have higher growth rates than EM-LHDWs.

The real frequency at maximum growth, $\omega_{\rm max}/\omega_{\rm LH}$, is shown in Figure 4(b). In most cases, $\omega_{\rm max}/\omega_{\rm LH}$ scales with the growth rate and can even exceed unity at very large $u_{0x}/C_{\rm s}$. While this might appear inconsistent with the conventional expectation that LHDWs remain below the lower-hybrid frequency, such cases are unlikely in realistic plasmas, where $u_{0x}/C_{\rm s}$ rarely exceeds $\sim$5.

The angular dependence is presented in Figure 4(c), where $\theta_{\rm max}$ denotes the angle between $\boldsymbol{k}$ and $\boldsymbol{B}_0$ for the most unstable mode. The mode becomes increasingly oblique as both β_e and $u_{0x}/C_{\rm s}$ rise (H. Ji et al. 2005). However, for $u_{0x}/C_{\rm s} \lesssim 1.5$, this effect is of limited relevance because the wave is already marginally unstable once $\beta_{\rm e} \gtrsim 1$.

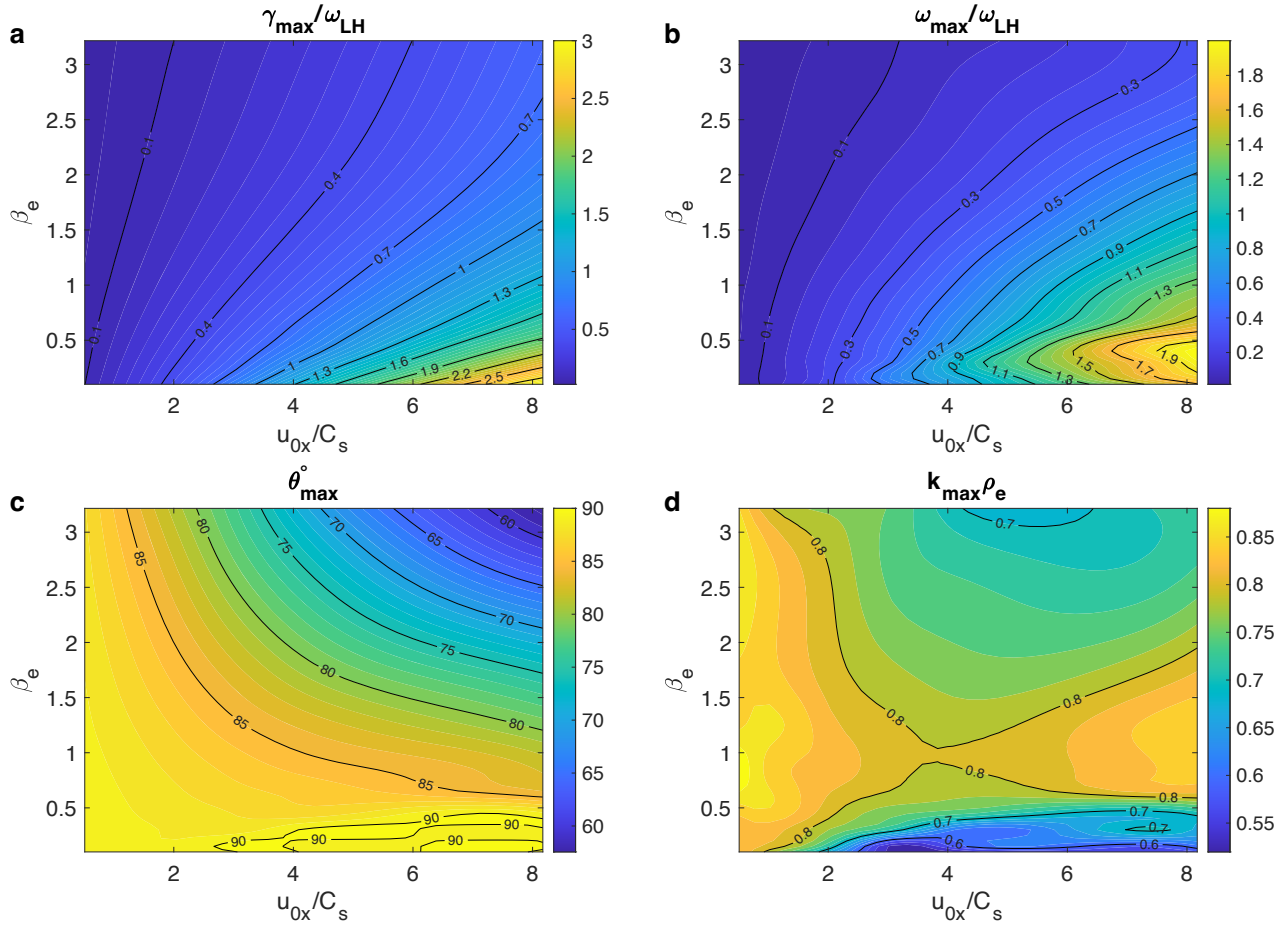

Figure 4. Parameter (β_e and u_{0x}/C_s) dependence of the most unstable LHDW mode. (a) Normalized maximum growth rate, γ_{max}/ω_{LH}, showing an increase with u_{0x}/C_s and a decrease with β_e, indicating stronger growth for ES-LHDWs. (b) Real frequency at maximum growth, ω_{max}/ω_{LH}, generally scaling with γ_{max}/ω_{LH} and occasionally exceeding unity for large u_{0x}/C_s. (c) θ of the mode with the maximum growth rate (θ_{max}). LHDWs become more oblique at higher β_e and larger u_{0x}/C_s. (d) Normalized wavenumber with the maximum growth rate, $k_{max}\rho_e$, highlighting two regimes: low β_e and high u_{0x}/C_s favor smaller wavenumbers ($k_{max}\rho_e \sim 0.5$), while moderate-to-high β_e yields slightly decreasing $k_{max}\rho_e$ (~0.7-0.85), largely independent of the type of the mode.

Finally, Figure 4(d) shows the variation of $k_{max}\rho_e$. Two regimes are evident. At high u_{0x}/C_s and low β_e, the mode with the maximum growth rate has relatively small wavenumbers (dark blue region with $k_{max}\rho_e \sim 0.5$). Across the broader regime of moderate to high β_e, $k_{max}\rho_e$ decreases monotonically with β_e, but remains within a narrow range of ~0.7–0.85. This indicates that the characteristic wavelength increases as β_e increases, though the shift is modest and largely independent of whether the mode is electrostatic or electromagnetic.

These results challenge the conventional scaling of $k\rho_e \sim 1$ for ES-LHDWs and $k\sqrt{\rho_e\rho_i} \sim 1$ for EM-LHDWs (W. Daughton 2003; V. Roytershteyn et al. 2012). Instead, the more general scaling is $k\rho_e \sim 1$ for both, with significantly longer wavelengths for ES-LHDWs appearing only in a limited regime (very high u_{0x}/C_s and $\beta_e \lesssim 0.5$). The apparent discrepancy with earlier studies (W. Daughton 2003; V. Roytershteyn et al. 2012) arises from the definition of ρ_e and ρ_i. In these works, where the global current sheet structure is considered, the asymptotic magnetic field strength in the upstream of magnetic reconnection is used to define the gyroradii. In our local model, however, ρ_e and ρ_i are defined using the local magnetic field strength. Near the electron diffusion region, where the local field is strongly reduced, this choice can yield $k\rho_e \sim 1$ while still being consistent with $k\sqrt{\rho_e\rho_i} \sim 1$ under the global definition. As illustrated in Figure 2(b), the physical wavelength of the EM-LHDW remains nearly unchanged compared with the reference (ES-LHDW) case when β_e is increased through density. Thus, it is more accurate to state that both ES-LHDWs and EM-LHDWs follow the general scaling $k\rho_e \sim 1$ when the gyroradii are defined with the local magnetic field strength.

Although the present study is limited to linear stability analysis, it is useful to briefly discuss the expected saturation amplitude and energy conversion efficiency of LHDWs. Previous simulation studies of electrostatic LHDWs have shown that saturation occurs through a balance between the free energy in the cross-field drift and the wave energy (D. Winske & P. Liewer 1978; J. Ng et al. 2024). In the electrostatic limit, the saturation electric-field amplitude can be estimated by equating the available free energy to the wave energy density, yielding values that agree reasonably well with particle-in-cell simulation results.

The saturation amplitudes of both ES-LHDWs and EM-LHDWs can be estimated using the same heuristic argument. The time-averaged total wave energy density in a dispersive plasma is given by (T. Stix 1992)

$$W = \frac{1}{4}\left[\epsilon_0 \delta \boldsymbol{E}^* \cdot \frac{\partial}{\partial \omega}(\omega \boldsymbol{\epsilon}_h) \cdot \delta \boldsymbol{E} + \frac{1}{\mu_0}\delta \boldsymbol{B}^* \cdot \delta \boldsymbol{B}\right], \quad (1)$$

where ϵ_0 is the permittivity of free space, $\boldsymbol{\epsilon}_h$ is the Hermitian part of the relative dielectric tensor $\boldsymbol{\epsilon}$, and $\delta\boldsymbol{E}$ and $\delta\boldsymbol{B}$ are the wave electric- and magnetic-field amplitudes, respectively. The dielectric tensor $\boldsymbol{\epsilon}$ is directly related to the conductivity tensor $\boldsymbol{\sigma}$, which relates the wave-induced current density to the electric field through $\delta\boldsymbol{J} = \boldsymbol{\sigma} \cdot \delta\boldsymbol{E}$. By combining Ampère's law and the definition of the displacement field $\boldsymbol{D} = \epsilon_0\boldsymbol{\epsilon} \cdot \boldsymbol{E}$, one obtains

$$\boldsymbol{\epsilon} = \boldsymbol{I} + \frac{i\boldsymbol{\sigma}}{\epsilon_0\omega}, \tag{2}$$

where $\boldsymbol{I}$ is the unit tensor. Substituting this expression into the wave-energy formula yields

$$W = \frac{1}{4}\left[\epsilon_0\delta\boldsymbol{E}^* \cdot \delta\boldsymbol{E} + \delta\boldsymbol{E}^* \cdot \frac{\partial}{\partial\omega}(i\boldsymbol{\sigma})_h \cdot \delta\boldsymbol{E} + \frac{1}{\mu_0}\delta\boldsymbol{B}^* \cdot \delta\boldsymbol{B}\right], \tag{3}$$

where the second term on the right-hand side represents the kinetic energy of coherent particle oscillations and the potential energy associated with plasma polarization.

From the linear dispersion calculations (J. Yoo et al. 2020), the frequency derivative of the conductivity tensor can be evaluated directly for each mode. Using Faraday's law, $\omega\delta\boldsymbol{B} = \boldsymbol{k} \times \delta\boldsymbol{E}$, the magnetic-field fluctuations can be expressed in terms of $\delta\boldsymbol{E}$, allowing W to be written entirely in terms of the electric-field amplitude. Assuming that the mode with the maximum linear growth rate dominates the nonlinear evolution and that the linear relation between $\delta\boldsymbol{B}$ and $\delta\boldsymbol{E}$ remains approximately valid up to saturation, as evidenced in the laboratory (J. Yoo et al. 2024, 2025), one can estimate the saturated electric-field amplitude by equating the total wave energy density W to the available free energy source, $m_e n_e u_{0x}^2/2$.

For broader applicability, it is more useful to discuss the results in terms of normalized quantities rather than absolute field amplitudes. For example, we define the saturated electric-field energy normalized to the available wave free energy, or the fraction of electric-field energy of the total wave energy, $\overline{W}_E$, as

$$\bar{W}_E = \frac{\epsilon_0\delta\boldsymbol{E}^*_{\rm sat} \cdot \delta\boldsymbol{E}_{\rm sat}}{2m_e n_e u_{0x}^2} \approx \left[1 + \frac{\delta\boldsymbol{E}^* \cdot \frac{\partial}{\partial\omega}(i\boldsymbol{\sigma})_h \cdot \delta\boldsymbol{E} + \frac{1}{\mu_0}\delta\boldsymbol{B}^* \cdot \delta\boldsymbol{B}}{\epsilon_0\delta\boldsymbol{E}^* \cdot \delta\boldsymbol{E}}\right]^{-1}, \tag{4}$$

where $\delta\boldsymbol{E}_{\rm sat}$ denotes the saturated electric-field amplitude. The right-hand side of the above equation can be evaluated using the linear field-particle relations for the mode with the maximum growth rate. This quantity provides a direct measure of the fraction of the available free energy converted into the electric-field energy at saturation. In an analogous manner, the normalized saturated magnetic-field energy ($\overline{W}_B$) can also be computed. In addition, other useful dimensionless quantities such as $|\delta\boldsymbol{B}_{\rm sat}|/B_0$ and $|\delta\boldsymbol{E}_\perp|/|\delta E_\parallel|$ can be evaluated for the mode with the maximum growth rate. Here, $\delta\boldsymbol{B}$sat denotes the saturated magnetic-field fluctuation amplitude, and $\delta\boldsymbol{E}\perp$ and $\delta E_\parallel$ denote the fluctuating electric-field components perpendicular and parallel to $\boldsymbol{B}_0$, respectively. These normalized quantities allow more direct comparison across different plasma parameters and provide a more general characterization of LHDW saturation behavior.

Figure 5(a) shows a contour plot of $\log \overline{W}_E$, the fraction of the available free energy converted into electric-field energy at saturation. The highest values of the electric-field energy fraction (around $10^{-2.8}$, or ~0.16%) occur at the lowest β_e values ($\beta_e < 0.5$). As β_e increases toward 3, $\overline{W}_E$ decreases substantially to values of order $10^{-4.4}$ (or ~0.004%). This provides a direct quantitative confirmation that increasing electron beta strongly suppresses the saturation level of the electric field. By contrast, $\overline{W}_E$ is only weakly dependent on u_{0x}/C_s over most of the parameter range.

It is also important to note that even at its peak, the electric-field energy represents only a very small fraction of the total available free energy (well below 1%), indicating that plasma kinetic energy and magnetic fluctuations dominate the overall energy budget. For the reference case, the estimated saturated amplitude is $|\delta\boldsymbol{E}_{\rm sat}| \simeq 9$ mV m^{-1}. For similar plasma parameters, space observations report electric-field amplitudes of order 10 mV m^{-1} (J. Yoo et al. 2020), in good agreement with this estimate.

Figure 5(b) shows the normalized saturated magnetic-field energy fraction, $\overline{W}_B$, as a function of β_e and u_{0x}/C_s. For low electron beta ($\beta_e < 0.5$), $\overline{W}_B$ remains small ($\overline{W}_B < 0.2$), indicating that the mode is predominantly electrostatic. In this regime, the majority of the wave energy resides in the wave-associated particle kinetic response. As β_e increases, however, $\overline{W}_B$ rises sharply, reaching values above 0.6 for $\beta_e \approx 2.0$. This confirms that at higher beta, the LHDW becomes strongly electromagnetic, with more than half of the wave energy residing in magnetic-field fluctuations.

The conversion efficiency into magnetic-field energy also depends on the drift magnitude. For weak drifts ($u_{0x}/C_s < 2$), the magnetic component is suppressed regardless of β_e. The maximum magnetic energy conversion occurs at intermediate to high drift velocities ($u_{0x}/C_s \approx 4$–8), where the available free energy is most effectively coupled into the electromagnetic components of the mode. A clear peak in magnetic energy partition is centered around $\beta_e \approx 1.5$–2.5 and $u_{0x}/C_s \approx 5$. Beyond this β_e range, the growth rate of the LHDW decreases because of increasing kinetic stiffness, which may explain the gradual tapering of $\overline{W}_B$ at very high beta values seen in the upper-right portion of the plot.

Figure 5(c) shows $|\delta\boldsymbol{B}_{\rm sat}|/B_0$ as a function of β_e and u_{0x}/C_s. Unlike the electric-field energy fraction $\overline{W}_E$, which is suppressed at high beta, the normalized magnetic perturbation amplitude $|\delta\boldsymbol{B}_{\rm sat}|/B_0$ increases systematically with both β_e and u_{0x}/C_s. At low $\beta_e < 1$ and weak drifts ($u_{0x}/C_s < 3$), the magnetic fluctuations are negligible ($|\delta\boldsymbol{B}_{\rm sat}|/B_0 < 0.05$), reinforcing the quasi-electrostatic character of the LHDW in this regime. In the high-β_e and high-u_{0x}/C_s region (upper right), the fluctuations exceed $0.5B_0$. This indicates that the waves are no longer small perturbations but can significantly distort the local magnetic-field structure at saturation.

Such large-amplitude magnetic perturbations are sufficient to enable magnetic particle trapping and potentially promote secondary magnetic reconnection or field-line stochasticity, both of which are efficient mechanisms for converting wave energy into particle heat. This suggests that EM-LHDWs may

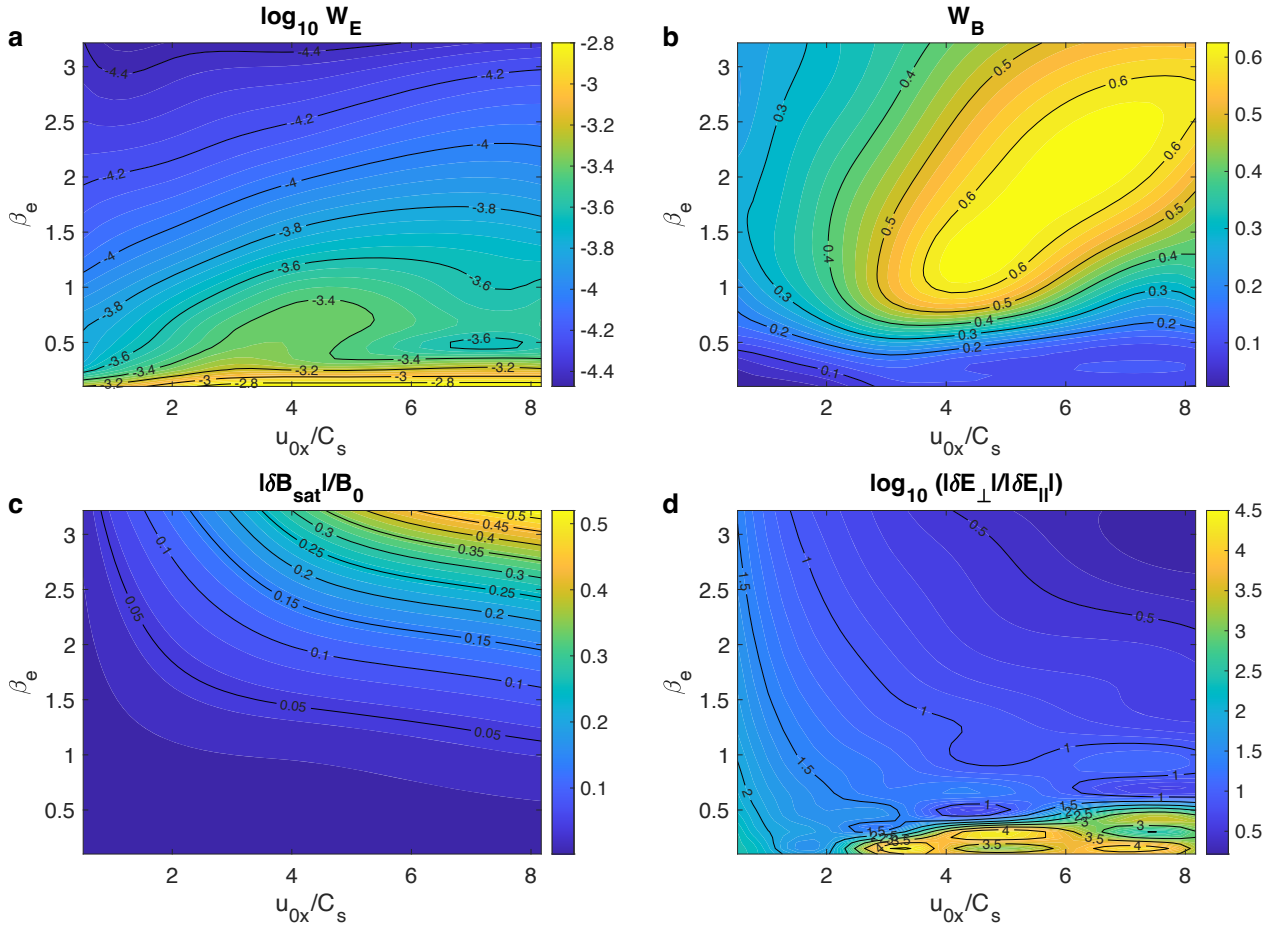

Figure 5. Parameter dependence of normalized saturation properties of lower-hybrid drift waves as functions of β_e and u_{0x}/C_s, evaluated for the mode with the maximum linear growth rate. (a) $\log \overline{W_E}$, the fraction of the available free energy converted into electric-field energy at saturation. The electric-field energy fraction is largest at low β_e and decreases strongly with increasing β_e. (b) $\overline{W_B}$, the fraction of the wave energy residing in magnetic-field fluctuations at saturation. The magnetic energy fraction increases rapidly with β_e, indicating a transition from predominantly electrostatic to strongly electromagnetic behavior. (c) Normalized magnetic-field fluctuation amplitude, $|\delta \boldsymbol{B}_{\rm sat}|/B_0$, showing systematic growth with both β_e and u_{0x}/C_s, and reaching order-unity values in the high-β_e, high-drift regime. (d) Ratio of perpendicular to parallel electric-field amplitudes, $|\delta \boldsymbol{E}_\perp|/|\delta E_\parallel|$, where $E_\parallel$ denotes the component parallel to the equilibrium magnetic field $\boldsymbol{B}_0$. The ratio decreases sharply with increasing β_e, indicating the emergence of strong parallel electric-field fluctuations in the electromagnetic regime.

contribute to turbulent reconnection and associated particle energization in strongly driven environments such as the magnetotail (R. E. Ergun et al. 2020a, 2020b).

Figure 5(d) shows the ratio $|\delta \boldsymbol{E}_\perp|/|\delta E_\parallel|$ as a function of β_e and u_{0x}/C_s. At low electron beta ($\beta_e < 0.5$), this ratio is extremely large, indicating that the LHDW electric field is almost entirely perpendicular to the magnetic field, with a negligible parallel component. As β_e increases, the ratio decreases sharply across all drift velocities. In the high-beta regime ($\beta_e > 2.5$), the ratio falls to values of order 0.5 on the logarithmic scale (corresponding to a factor of $\sim$3), indicating that the perpendicular and parallel electric-field components become comparable.

Most importantly, as the plasma becomes increasingly electromagnetic and $|\delta \boldsymbol{B}_{\rm sat}|$ approaches B_0 (as seen in panel (c)), the electric-field components satisfy $|\delta \boldsymbol{E}_\perp| \sim |\delta E_\parallel|$, because the effective parallel direction is no longer aligned with the equilibrium magnetic field. In this regime, the wave-induced magnetic perturbations significantly distort the local field geometry, so that a substantial component of the electric field becomes parallel to the total magnetic field. This implies that the saturated state of EM-LHDWs is characterized by strong parallel electric-field fluctuations, which are particularly effective at driving electron acceleration and parallel heating through wave–particle interactions.

We emphasize that this saturation level should be interpreted as a rough estimate based on a heuristic quasi-linear argument. The present approach neglects nonlinear effects such as mode coupling, spectral energy transfer, particle trapping, and modification of the background distribution function, all of which can influence the true saturation amplitude. Nevertheless, the reasonable agreement with observations suggests that the linear growth rates and wave energetics identified here capture the correct physical scaling of LHDW amplitudes in a quasi-linear state.

These results indicate that ES-LHDWs are generally more effective than EM-LHDWs at generating anomalous resistivity and wave–particle interactions in the linear and weakly nonlinear regimes. This follows directly from their larger electric-field amplitudes, since wave–particle interaction strength, momentum exchange, and effective anomalous resistivity scale with the magnitude of the fluctuating electric field. Stronger electric fields therefore lead to more efficient electron scattering, enhanced energy diffusion in velocity space, and greater conversion of drift kinetic energy into electron thermal energy. This interpretation is consistent with

both space and laboratory observations (J. Yoo et al. 2020, 2024; N. Ahmadi et al. 2025; J. Yoo et al. 2025).

At the same time, our results suggest that EM-LHDWs may become an efficient channel for particle heating in the strongly nonlinear regime. As shown in Figure 5, EM-LHDWs can generate magnetic perturbations comparable to the background field and strong parallel electric fields, $|\delta E_{\parallel}| \sim |\delta \boldsymbol{E}\perp|$. In this regime, stochastic magnetic field lines and large-amplitude $E_{\parallel}$ fluctuations can enable rapid parallel electron acceleration, magnetic trapping, and enhanced cross-field transport, leading to efficient particle heating even when the electric-field energy fraction remains small. This is consistent with laboratory evidence of electron heating during strong EM-LHDWs observed in antiparallel reconnection current sheets (H. Ji et al. 2004). Moreover, these results suggest a complementary role for EM-LHDWs in strongly driven plasmas, where nonlinear magnetic fluctuations and parallel electric fields dominate the energy conversion process.

4. Discussion

Our results provide a unified framework for understanding the stability and characteristic properties of LHDWs across a wide range of plasma conditions. By systematically solving the LHDW dispersion relation, we have clarified how their behavior depends on two key dimensionless control parameters: the electron beta (β_e) and the normalized perpendicular electron drift velocity (u_{0x}/C_s). This framework resolves several long-standing ambiguities in the literature and helps reconcile differences between ES-LHDW and EM-LHDW observations.

First, our analysis shows that ES-LHDWs and EM-LHDWs are not distinct modes but rather the same drift wave with different characteristics. At low β_e and moderate u_{0x}/C_s, the mode with the maximum growth rate is predominantly electrostatic, with high growth rates and nearly perpendicular propagation. As β_e increases, the mode becomes more oblique, the growth rate decreases, and magnetic field fluctuations grow in importance, giving rise to EM-LHDW characteristics. This continuous transition demonstrates that the two wave types are manifestations of the same drift wave whose character is set by plasma and field parameters rather than by fundamentally different physics.

Second, the growth rate is controlled primarily by the competition between u_{0x}/C_s and β_e. Larger u_{0x}/C_s enhances the mode by increasing the available free energy, while larger β_e suppresses it through electron dynamics and Landau damping. Importantly, electron temperature anisotropy further modifies stability, with $T_{e||}$ playing a particularly strong role via parallel Landau damping.

Third, our results refine the conventional scaling laws for LHDW wavelengths. The most unstable modes occur at $k\rho_e \sim 0.8$, largely independent of whether the mode is electrostatic or electromagnetic. This contrasts with the widely cited scalings of $k\rho_e \sim 1$ for ES-LHDWs and $k\sqrt{\rho_e \rho_i} \sim 1$ for EM-LHDWs. Only under a restricted set of conditions (very high u_{0x}/C_s and low β_e) do ES-LHDWs extend to significantly longer wavelengths. These findings suggest that the characteristic scale of LHDWs is universal when the gyroradii are defined with the local magnetic field strength. This result is also consistent with space observations: C. Norgren et al. (2012) reported $k\rho_e \sim 0.5$–1 for 10 events in the magnetotail, and J. Yoo et al. (2020) found $k\rho_e \sim 0.7$ at the magnetopause.

Finally, our comparison with the classical model of R. Davidson et al. (1977) highlights the importance of electromagnetic effects (X. Yu et al. 2021). Retaining Faraday's induction law, rather than closing with Poisson's equation, produces both the correct frequency scaling and realistic growth rates. This result explains why modern observations of LHDWs consistently show correlated magnetic and electric field fluctuations, even in regimes traditionally thought to be electrostatic.

Moreover, the quasi-linear saturation estimates presented in Figure 5 extend the linear stability analysis into a physically meaningful nonlinear context and clarify how LHDWs partition energy and heat particles across different parameter regimes. Together with the linear results, they show that the control parameters β_e and u_{0x}/C_s govern not only wave growth and propagation but also saturation amplitude, energy conversion efficiency, and wave polarization. In particular, the transition from electrostatic to electromagnetic behavior with increasing β_e is accompanied by a systematic shift of wave energy from electric fields into magnetic fluctuations and particle kinetic responses. This provides a unified framework for understanding why ES-LHDWs are typically associated with strong anomalous resistivity and electron heating near sharp gradients, whereas EM-LHDWs dominate in high-β_e environments characterized by intense magnetic and electric fluctuations along the direction parallel to the magnetic field.

More broadly, these results imply that LHDWs can play qualitatively different but complementary roles in collisionless plasma energy conversion depending on the local plasma conditions. In low-β_e regimes, large-amplitude perpendicular electric fields enable efficient wave–particle scattering and drift-energy dissipation, while in high-β_e regimes, strong magnetic perturbations and parallel electric fields enable efficient particle acceleration and heating through stochastic field-line topology and parallel energization. This dual role provides a natural explanation for the diverse observational signatures of LHDWs across boundary layers, shear flows, and turbulent plasma interfaces, and underscores their importance as a universal kinetic dissipation mechanism in collisionless plasmas.

It is also important to acknowledge the limitations of the local linear model used here. The analysis assumes a clear scale separation in which the characteristic scale length of the system, such as the current sheet, is much larger than the electron gyroradius, allowing gradients to be treated as locally uniform and permitting the neglect of wave propagation along the density gradient. However, in regimes where the relevant scale length approaches ρ_e, such as in very thin layers (e.g., electron diffusion regions or shock wave fronts) or strongly kinetic environments, these assumptions may not be valid. In such cases, nonlocal effects and finite-size geometry are expected to become important, and the present model may no longer provide quantitatively accurate predictions for the stability and the propagation of LHDWs.

Another important limitation of the present study is that it relies on a linearized treatment of fundamental equations, thereby neglecting nonlinear effects. In real plasmas, large-amplitude waves can lead to wave–wave interactions, mode coupling, particle trapping, and modifications of the background distribution function, all of which can significantly alter the growth rate, saturation, and spectral properties of LHDWs. Consequently, the linear predictions presented here

provide an accurate description only for the early stages of the wave or for weakly perturbed plasmas, despite some apparent successes of quasi-linear treatments (R. Kulsrud et al. 2005; J. Yoo et al. 2024; N. Ahmadi et al. 2025).

Looking ahead, incorporating nonlinear effects and nonlocal geometry will be an essential next step. Such extensions would enable quantitative predictions of saturation amplitudes, anomalous transport rates, and the interaction of LHDWs with other microinstabilities in thin boundary layers, leading to a more complete understanding of their role in fundamental processes in collisionless plasma such as magnetic reconnection.

Acknowledgments

This work was supported by DOE Contract No. DEAC0209CH11466, NASA grants Nos. NNH20ZDA001N, 80HQTR21T0060, 80NSSC21K1462, 80NSSC21K1795, 80HQTR21T0105, and 80NSSC24K0094, and the NASA MMS Project. The data that support the findings of this study are openly available in the Princeton Data Commons (doi:10.34770/5hgn-5684; J. Yoo 2026).

Author Contributions

J.Y. conceived the research concept, performed the dispersion relation calculations, led the primary data interpretation, and wrote the initial manuscript draft. H.J. contributed to data interpretation and manuscript development. J.N., L.C., P.S., S. B., K.M., E.J., and A.R. participated in the physics discussions and contributed to the writing and refinement of the manuscript.

ORCID iDs

Jongsoo Yoo https://orcid.org/0000-0003-3881-1995
Hantao Ji https://orcid.org/0000-0001-9600-9963
Jonathan Ng https://orcid.org/0000-0002-5183-3577
Li-Jen Chen https://orcid.org/0000-0002-4768-189X
Peiyun Shi https://orcid.org/0000-0002-7129-278X
Sayak Bose https://orcid.org/0000-0001-8093-9322
Kush Maheshwari https://orcid.org/0000-0003-1198-4685
Euichan Jung https://orcid.org/0000-0001-5108-8055
Adam Robbins https://orcid.org/0009-0005-5560-2003

References

Ahmadi, N., Ji, H., Yoo, J., et al. 2025, JGRA, 130, e2024JA033238
Bale, S. D., Mozer, F. S., & Phan, T. 2002, GeoRL, 29, 2180
Carter, T., Ji, H., Trintchouk, F., Yamada, M., & Kulsrud, R. 2002a, PhRvL, 88, 015001
Carter, T., Yamada, M., Ji, H., Kulsrud, R., & Trintchouk, F. 2002b, PhPl, 9, 3272
Carter, T. A., Ji, H., Trintchouk, F., Yamada, M., & Kulsrud, R. M. 2001, PhRvL, 88, 015001
Chen, L.-J., Wang, S., Hesse, M., et al. 2019, GeoRL, 46, 6230
Chen, L.-J., Wang, S., Le Contel, O., et al. 2020, PhRvL, 125, 025103
Daughton, W. 2003, PhPl, 10, 3103
Davidson, R., Gladd, N., Wu, C., & Huba, J. 1977, PhFl, 20, 301
Ergun, R. E., Ahmadi, N., Kromyda, L., et al. 2020a, ApJ, 898, 153
Ergun, R. E., Ahmadi, N., Kromyda, L., et al. 2020b, ApJ, 898, 154
Feng, B., Ouyang, Z., Yu, X., et al. 2025, GeoRL, 52, e2025GL116142
Graham, D. B., Khotyaintsev, Y. V., Norgren, C., et al. 2017, JGRA, 122, 517
Graham, D. B., Khotyaintsev, Y. V., Norgren, C., et al. 2019, JGRA, 124, 8727
Graham, D. B., Khotyaintsev, Y. V., Vaivads, A., et al. 2022, NatCo, 13, 2954
Guo, Z. Z., Liu, Y. Y., Fu, H. S., et al. 2022, ApJ, 933, 128
Ji, H., Kulsrud, R., Fox, W., & Yamada, M. 2005, JGRA, 110, A08212
Ji, H., Terry, S., Yamada, M., et al. 2004, PhRvL, 92, 115001
Kulsrud, R., Ji, H., Fox, W., & Yamada, M. 2005, PhPl, 12, 082301
Ng, J., Yoo, J., Chen, L.-J., Bessho, N., & Ji, H. 2024, PhRvR, 6, L042072
Norgren, C., Vaivads, A., Khotyaintsev, Y. V., & André, M. 2012, PhRvL, 109, 055001
Ouyang, Z., Li, H., Yuan, Z., et al. 2022, GeoRL, 49, e2022GL100485
Roytershteyn, V., Daughton, W., Karimabadi, H., & Mozer, F. S. 2012, PhRvL, 108, 185001
Roytershteyn, V., Dorfman, S., Daughton, W., et al. 2013, PhPl, 20, 061212
Shukla, P. K., & Mamun, A. A. 2002, JGRA, 107, 1401
Silin, I., Büchner, J., & Vaivads, A. 2005, PhPl, 12, 062902
Stix, T. 1992, Waves in Plasmas (American Institute of Physics)
Treumann, R. A. 2009, A&ARv, 17, 409
Winske, D., & Liewer, P. 1978, PhFl, 21, 1017
Yoo, J. 2026, Stability and Characteristics of Lower-Hybrid Drift Waves in Magnetic Reconnection: Dependence on Electron Beta and Perpendicular Drift, Princeton Plasma Physics Laboratory, Princeton Univ., doi:10.34770/5hgn-5684
Yoo, J., Hu, Y., Ji, J.-Y., et al. 2022, PhPl, 29, 022109
Yoo, J., Ji, H., Shi, P., et al. 2025, PhPl, 32, 062114
Yoo, J., Ji, J.-Y., Ambat, M. V., et al. 2020, GeoRL, 47, e2020GL087192
Yoo, J., Na, B., Jara-Almonte, J., et al. 2017, JGRA, 122, 9264
Yoo, J., Ng, J., Ji, H., et al. 2024, PhRvL, 132, 145101
Yoo, J., Yamada, M., Ji, H., et al. 2014, PhRvL, 113, 095002
Yoon, P. H., & Lui, A. T. Y. 2004, JGRA, 109, A02210
Yoon, P. H., & Lui, A. T. Y. 2007, JGRA, 112, A06207
Yu, X., Yuan, Z., Yao, F., Ouyang, Z., & Wang, D. 2021, JGRA, 126, e2021JA029759